

# Fabrication of hierarchical Sn-doped ZnO nanorod arrays through sonicated sol–gel immersion for room temperature, resistive-type humidity sensor applications

A.S. Ismail<sup>a</sup>, M.H. Mamat<sup>a,b,\*</sup>, N.D. Md. Sin<sup>a</sup>, M.F. Malek<sup>a,b</sup>, A.S. Zoofakar<sup>a</sup>, A.B. Suriani<sup>c</sup>, A. Mohamed<sup>c</sup>, M.K. Ahmad<sup>d</sup>, M. Rusop<sup>a,b</sup>

<sup>a</sup> NANO-ElecTronic Centre (NET), Faculty of Electrical Engineering, Universiti Teknologi MARA (UiTM), 40450 Shah Alam, Selangor, Malaysia

<sup>b</sup> NANO-SciTech Centre (NST), Institute of Science (IOS), Universiti Teknologi MARA (UiTM), 40450 Shah Alam, Selangor, Malaysia

<sup>c</sup> Nanotechnology Research Centre, Faculty of Science and Mathematics, Universiti Pendidikan Sultan Idris (UPSI), 35900 Tanjung Malim, Perak, Malaysia

<sup>d</sup> Microelectronic and Nanotechnology – Shamsuddin Research Centre (MiNT-SRC), Faculty of Electrical and Electronic Engineering, Universiti Tun Hussein Onn Malaysia (UTHM), 86400 Batu Pahat, Johor, Malaysia

## ARTICLE INFO

### Article history:

Received 1 February 2016

Received in revised form

1 March 2016

Accepted 9 March 2016

Available online 10 March 2016

### Keywords:

Humidity sensor

Sn-doped ZnO

Nanorod

Immersion

Structural properties

## ABSTRACT

Hierarchical tin (Sn)-doped zinc-oxide (ZnO) nanorod arrays (SZO) were deposited onto Al-doped ZnO-coated glass substrate by using a sonicated sol–gel immersion method for resistive-type humidity sensor applications. X-ray diffraction patterns revealed that the deposited SZO arrays exhibit a wurtzite structure. SZO possessed smaller average diameter, crystallite size, and thickness than the undoped sample did. The SZO film also exhibited compressive strain and tensile stress values of  $-0.033\%$  and  $77\text{ MPa}$ , respectively. Our result showed the sensitivity of the SZO based-sensor improved compared with that of the undoped ZnO, with values of 3.41 and 1.41 at 40% to 70% RH and 70% to 90% RH, respectively. The response and recovery times of the SZO based humidity sensor improved to 230 and 30 s, respectively. All these results indicated that SZO had high potential for humidity-sensor applications.

© 2016 Elsevier Ltd and Techna Group S.r.l. All rights reserved.

## 1. Introduction

The monitoring and detection of humidity are of considerable importance for various technological purposes, including electronic device fabrication, food technology, health care, and industrial chemicals. The most common material types used for humidity sensors are metal oxide semiconductors because these materials exhibit ease in fabrication, controllable size and morphology, capability for surface modification, and chemical stability. Compared with other sensing materials, metal oxide semiconductors are characterized by low costs, simple construction, small size, and easy installation. Zinc oxide (ZnO), a wide bandgap ( $\sim 3.3\text{ eV}$ ) *n*-type semiconductor with high chemical/physical stability and unique electrical and optical properties, has emerged as an important material in the fields of sensors, field electron emission, and solar cells [1–4]. Extensive scientific and technological efforts have been devoted to the preparation of ZnO nanostructure-based humidity sensors to enhance sensitivity, response/recovery time,

selectivity, and stability [5–7]. Recently, ordered structured semiconductor metal oxides, such as ZnO nanorod arrays, which provide several advantages, such as extensive surface area, high surface-to-volume ratio, and high electron mobility, have been extensively investigated in terms of the outlining and development of highly sensitive humidity sensors. One-dimensional ZnO nanorod structure exhibits performance superior to nanoparticle films because the former yields a higher surface-to-volume ratio than the latter does; moreover, the structure provides a direct pathway for charge transport along the axis of ZnO arrays; as a result, electron–hole pair recombination possibilities are considerably reduced [8,9]. Various synthesis approaches of ZnO nanorod arrays include solution-based processes [10–13], chemical vapor deposition (CVD) [14], sputtering [15], and metalorganic CVD [16]. Among these approaches, solution-based methods have emerged as a promising method because of their simplicity, low cost, and ability to produce high-quality ZnO nanorod arrays.

Numerous types of humidity sensors have been described. To date, various sensor types, such as capacitive [5], resistive [17], optical fiber [18], surface acoustic wave (SAW) [19], and quartz crystal microbalance (QCM) [20] have been used as humidity sensors. Resistive-type humidity sensors have received considerable attention because they are characterized by several

\* Corresponding author at: NANO-ElecTronic Centre (NET), Faculty of Electrical Engineering, Universiti Teknologi MARA (UiTM), 40450 Shah Alam, Selangor, Malaysia.

E-mail address: [mhmamat@salam.uitm.edu.my](mailto:mhmamat@salam.uitm.edu.my) (M.H. Mamat).

advantages, such as easy preparation, low cost, direct current electrical conductivity, and simple application circuit [21]. Resistive-type humidity sensing materials include metal oxide semiconductors, polymers, and polyelectrolytes. For resistive-type ZnO-based humidity sensors, the use of pristine ZnO sensors is associated with few drawbacks, such as lagging change in resistance values at higher relative humidity (RH) because of the high resistivity of the material. As a consequence, this condition limits their practical applications. To overcome this problem and to improve the properties of ZnO, researchers should subject these materials to doping. Several metals, such as silver (Ag), iron (Fe), aluminum (Al), and tin (Sn), have been doped ZnO materials [22–25]. We investigated Sn because of its promising dopant characteristics; for instance, Sn can enhance conductivity because of double-ionized donors, which provide extra carriers, improve ZnO properties, such as field emission (FE) characteristics, and increase water adsorption for humidity-sensing applications [26–28]. For example, Hendi et al. investigated the effect of different concentration of Sn-doped ZnO-based QCM humidity sensor and found that crystallite size decreases when ZnO is doped with Sn [28]. They also observed that the performance of the QCM humidity sensor improves when ZnO is doped with Sn. However, other studies have demonstrated that Sn degrades sensor performance. For instance, Ates et al. prepared Sn-doped ZnO-based QCM humidity sensors with varying concentrations of Sn through a sol–gel method [29]. Their result suggested that crystallinity decreases as the Sn concentration increases. They also observed an increase in particle size upon Sn doping; as a result, frequency drifting is induced and humidity sensing capabilities are degraded.

Sn-doped ZnO film-based humidity sensors, particularly for QCM type humidity sensors, have been described. However, a detailed investigation has yet to be conducted on the properties of hierarchical Sn-doped ZnO nanorod arrays (SZO) in terms of structural and optical characteristics, such as crystallite size, stress/strain, and Urbach energy, particularly their effects on the humidity-sensing performance of resistive-type sensor configuration. Furthermore, SZO-based humidity sensors in a resistive configuration has not been widely studied. Therefore, this particular topic is of particular interest for understanding SZO behavior in terms of structural and optical properties, as well as their resulting humidity-sensing performance. In this contribution, a SZO-based humidity sensor was prepared via an efficient and simple sonicated sol–gel immersion method. Using this method, we fabricated the SZO-based humidity sensor to detect humidity at room temperature. A sensing system in various humidity levels was established, and sensor response was examined through electrical measurements, along with structural and optical characterizations to evaluate the properties of the fabricated sensor.

## 2. Experimental procedure

### 2.1. Preparation of ZnO seed layer

For the preparation of the seed layer, 0.4 M zinc acetate dihydrate ( $\text{Zn}(\text{CH}_3\text{COO})_2 \cdot 2\text{H}_2\text{O}$ ; 99.5% purity; Aldrich), 0.4 M monoethanolamine (MEA,  $\text{H}_2\text{NCH}_2\text{CH}_2\text{OH}$ ; 99.5% purity; Aldrich), 0.004 M aluminum nitrate nanohydrate ( $\text{Al}(\text{NO}_3)_3 \cdot 9\text{H}_2\text{O}$ ; 98% purity; Analar), and 2-methoxyethanol were used as a precursor, stabilizer, dopant source, and solvent, respectively. The reagents were mixed together and stirred on a hot plate stirrer at 80 °C for 3 h. Then, the solution was aged for 24 h at room temperature to obtain a homogeneous solution. The prepared solution was spin-coated on glass substrate at 3000 rpm for 1 min. Film-coated samples were then heated and dried at 150 °C for 10 min. The process was repeated five times to increase the thickness of the seed layer prior to final annealing at 500 °C for 1 h.

### 2.2. Preparation of undoped ZnO and SZO films

Nanorods were grown via a sonicated sol–gel immersion method. The solution was prepared using 0.1 M zinc nitrate hexahydrate ( $\text{Zn}(\text{NO}_3)_2 \cdot 6\text{H}_2\text{O}$ ; 98.5% purity; Schmidt), 0.1 M hexamethylenetetramine (HMT,  $\text{C}_6\text{H}_{12}\text{N}_4$ ; 99% purity; Aldrich), and 0.001 M tin (IV) chloride pentahydrate ( $\text{SnCl}_4 \cdot 5\text{H}_2\text{O}$ ; 98% purity; Aldrich) as a precursor, a stabilizer, and a dopant source, respectively. Undoped and Sn-doped solutions were prepared by mixing and dissolving the reagents in deionized (DI) water and then sonicating at 50 °C for 30 min. Afterward, the solutions were aged at room temperature for 3 h. Then, the solutions were poured into Schott bottles; the seed layer-coated glass substrates were placed at the bottom of the bottles. The bottles were then immersed in a water bath immersion tank at 95 °C for 2 h. Then, the samples were cleaned with DI water, heated, and dried at 150 °C for 10 min. The samples were annealed at 500 °C for 1 h. Gold (Au) metal contacts were deposited on top of the samples as electrodes at a thickness of 60 nm through sputtering (Emitech K550X) with aid of a physical mask. The configuration of the fabricated humidity sensor with SZO films is shown in Fig. 1.

### 2.3. Characterizations

The surface morphology/cross-sectional images and crystallinity properties of samples were characterized through field emission scanning electron microscopy (FESEM; JEOL JSM-7600F) and X-ray diffraction measurement (XRD; PANalytical X'Pert PRO), respectively. The prepared nanorods were characterized through compositional analysis by using an energy dispersive X-ray spectroscopy (EDX, INCA). The optical properties of the nanorod arrays were investigated using an ultraviolet–visible spectrophotometer (Varian Cary 5000). The sensor performance was determined using a humidity chamber (ESPEC-SH261) equipped with a sensor measurement system (Keithley 2400).

## 3. Result and discussion

The XRD patterns of undoped ZnO and SZO films are shown in Fig. 2. The XRD patterns of the films correspond to the four main diffraction peaks of ZnO, namely, (100), (002), (101), and (102). The observed peaks for the nanorod arrays are attributed to a polycrystalline structure with hexagonal wurtzite structure films (zincite phase JCPDS #36-1451) and exhibit a preferred (002) orientation. Sn peaks were not detected and secondary phases and clusters, such as  $\text{SnO}_2$ , were not formed. The intensity of the (002) peak exhibits a dominant diffraction; thus, the films are preferentially oriented along the *c*-axis and perpendicular to the substrate. High atomic density and surface energy minimization at

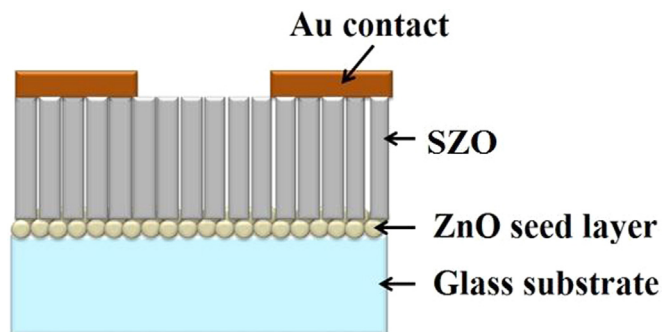


Fig. 1. Schematic of room temperature, resistive-type humidity sensor using SZO film.

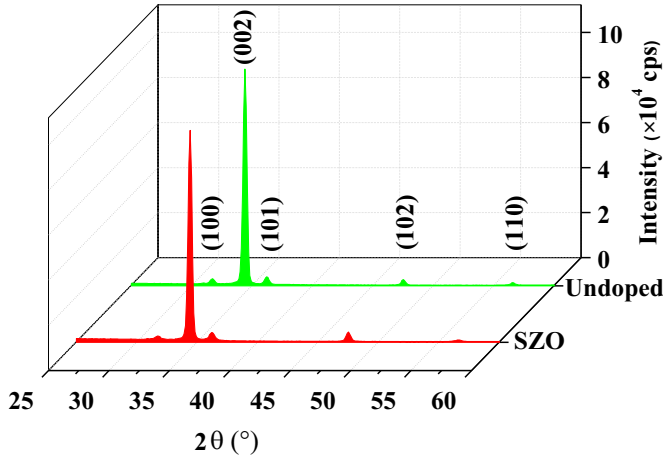


Fig. 2. XRD pattern of undoped ZnO and SZO films.

the *c*-axis orientation may explain the easy growth of along the *c*-axis orientation [30]. On the basis of the diffraction peaks, we also observed that the intensity of the preferred *c*-axis orientation (002) peaks is slightly decreased with Sn doping. This finding indicates that Sn atoms are successfully incorporated into the ZnO lattice.

The crystallite sizes,  $D_{(002)}$ , of the undoped ZnO and SZO were estimated from the full width at half maximum (FWHM,  $\beta$ ) of the (002) plane orientation peak by using the Scherrer's equation [31]:

$$D_{(002)} = \frac{0.94\lambda}{\beta \cos \theta} \quad (1)$$

where  $\lambda$  is the X-ray wavelength (1.54 Å),  $\beta$  is the FWHM in radians, and  $\theta$  is the diffraction angle.  $\beta$  and  $\theta$  were obtained from the diffraction peak of (002) plane orientation as shown in Table 1. On the basis of Scherrer estimation, we found that the crystallite sizes of the undoped ZnO and SZO were 30.7 and 27.8 nm, respectively. These results show that crystallite size slightly decreases with Sn doping. This behavior could be related to the difference between the ionic radii of  $\text{Zn}^{2+}$  (0.74 Å) and  $\text{Sn}^{4+}$  (0.69 Å) [32]. The reduction of crystallite size may reduce the average diameter and thickness of SZO.

The interplanar distance,  $d$ , and the lattice parameters,  $a$  and  $c$ , for the hexagonal structure of the undoped ZnO and SZO were determined by using the Bragg's equations [33,34]:

$$2d_{hkl} \sin \theta = n\lambda \quad (2)$$

$$\frac{1}{d_{hkl}^2} = \frac{4}{3} \left[ \frac{h^2 + hk + k^2}{a^2} \right] + \frac{l^2}{c^2} \quad (3)$$

where (*hkl*) represents Miller index,  $d_{hkl}$  represents the interplanar spacing for indices (*hkl*),  $a$  and  $c$  represent the lattice constants of the ZnO,  $n$  is the order of diffraction (usually  $n=1$ ),  $\lambda$  is the X-ray wavelength of Cu K $\alpha$  radiation (1.54 Å), and  $\theta$  is Bragg's angle.

Using Eqs. (2) and (3) with the first order approximation,  $n=1$ , the lattice constants  $a_{film}$  and  $c_{film}$  correspond to the (100) and (002) plane orientations, respectively, were determined. Eqs.

(2) and (3) can be simplified by the following equations [35]:

$$a_{film} = \frac{\lambda}{\sqrt{3} \sin \theta} \quad (4)$$

$$c_{film} = \frac{\lambda}{\sin \theta} \quad (5)$$

For  $a_{film}$ ,  $\theta$  is the diffraction angle corresponding to the (100) peak. For  $c_{film}$ ,  $\theta$  is the diffraction angle corresponding to the (002) peak. According to the XRD pattern, the diffraction angles  $2\theta$  at (002) and (100) plane orientations of undoped ZnO were 34.39° and 31.71°, respectively. On the other hand, the diffraction angles  $2\theta$  at (002) and (100) plane orientations of SZO were 34.42 and 31.82°, respectively. The calculated  $d_{hkl}$ ,  $a_{film}$ , and  $c_{film}$  of undoped ZnO were 2.6047, 3.2544, and 5.2093 Å, respectively, whereas those for SZO were 2.6025, 3.2434, and 5.2049 Å, respectively, as presented in Table 1. The results show that  $d_{hkl}$ ,  $a_{film}$ , and  $c_{film}$  decreased with Sn doping. These changes may occur because of lattice contraction when Sn replaces the Zn sites [36].

Moreover, the diffraction angle of SZO at (002) peak orientation shifted to a higher value, as shown in Table 1. The peak shift of SZO also provides an evidence for the partial substitution of Sn atoms into the ZnO lattice [37]. This finding may be attributed to the change in the crystallographic properties of thin films because of the difference between the ionic radii of  $\text{Sn}^{4+}$  and  $\text{Zn}^{2+}$ . Thus, the incorporation of Sn into ZnO lattice leads to a change in interplanar spacing (*d*-value) and an increase in the diffraction angle of (002) plane orientation according to the Bragg's equation [38]. This shift may be attributed to the deterioration of intrinsic stress in the crystal lattice. This shift is also consistent with that described by Ajili et al., who prepared a Sn-doped ZnO thin film through pulverization [39]. Other components affecting the crystal growth include the formation of stress and strain in the lattice because of the doping process. The strain  $\epsilon_{zz}$  in the ZnO nanorod along the *c*-axis can be calculated by using XRD data based on the biaxial strain model, as expressed in the following equation [40]:

$$\epsilon_{zz} = \frac{c_{film} - c_{bulk}}{c_{bulk}} \times 100\% \quad (6)$$

where  $c_{film}$  signifies the lattice parameter of the ZnO nanorod films and  $c_{bulk}$  is the unstrained lattice parameter for bulk ZnO (5.2066 Å). The positive and negative strain values represent the tensile strain when the film is stretched and the compressive strain when the film is compressed [41], respectively; by contrast, the residual stress of the film  $\sigma_{film}$  was obtained on the basis of the biaxial stress model expression [42]:

$$\sigma_{film} = \frac{2C_{13}^2 - C_{33}(C_{11} + C_{12})}{2C_{13}} \epsilon_{zz} \quad (7)$$

where  $C_{ij}$  are the elastic stiffness constants of bulk ZnO ( $C_{11}=208.8$  GPa,  $C_{12}=119.7$  GPa,  $C_{13}=104.2$  GPa, and  $C_{33}=213.8$  GPa) and  $\epsilon_{zz}$  is the lattice strain. This equation yields the following relationship for stress:  $\sigma_{film} = -233\epsilon_{zz}$  (GPa). The positive and negative values of stress represent the tensile stress and compressive stress, respectively [41]. On the basis of these equations, we obtained the strain/stress of the undoped ZnO and SZO of 0.051%/–119 MPa and –0.033%/77 MPa, respectively. After

Table 1

Diffraction angle at (002) and (100) plane orientations,  $\text{FWHM}_{(002)}$ , crystallite size, interplanar distance, lattice parameters, strain, and stress of undoped ZnO and SZO films.

Sample (GPa)	$2\theta$ at (002) plane (deg)	$2\theta$ at (100) plane (deg)	$\text{FWHM}_{(002)}$ (deg)	Crystallite size (nm)	Interplanar distance, <i>d</i> (Å)	$a_{film}$ (Å)	$c_{film}$ (Å)	Strain (%)	Stress (MPa)
Undoped ZnO	34.39	31.71	0.282	30.7	2.6047	3.2544	5.2093	0.051	–119
SZO	34.42	31.82	0.311	27.8	2.6025	3.2434	5.2049	–0.033	77

the sample was doped with Sn, the sample evidently exhibited compressive strain/tensile stress. In a previous report, doping with  $\text{Sn}^{4+}$  induces a change in crystal structure because the ionic radius of  $\text{Sn}^{4+}$  is smaller than that of  $\text{Zn}^{2+}$  [43]. Thus, Sn doping likely increases the relative stress and strain in the ZnO crystal. The stress and strain in the lattice may induce the formation of physical defects and dislocations in the crystal structure [44]. The dislocation in the crystal can be represented as dislocation density ( $\delta$ ), which refers to the length of dislocation lines per unit volume ( $\text{line}/\text{m}^3$ ). Dislocation densities can be obtained by using Williamson and Smallman estimation [45]:

$$\delta = \frac{1}{D^2} \quad (8)$$

where  $D$  refers to the crystallite size. The estimated dislocations for the undoped ZnO and SZO were  $1.06 \times 10^{15}$  and  $1.29 \times 10^{15}$  lines/ $\text{m}^3$ , respectively. The increase in the dislocation density of SZO suggests that doping Sn into ZnO nanorods enhances the relative compressive strain and tensile stress, which provide lattice imperfections.

The surface morphologies of the undoped ZnO and SZO are shown in Fig. 3(a) and (b), respectively. The images show that both

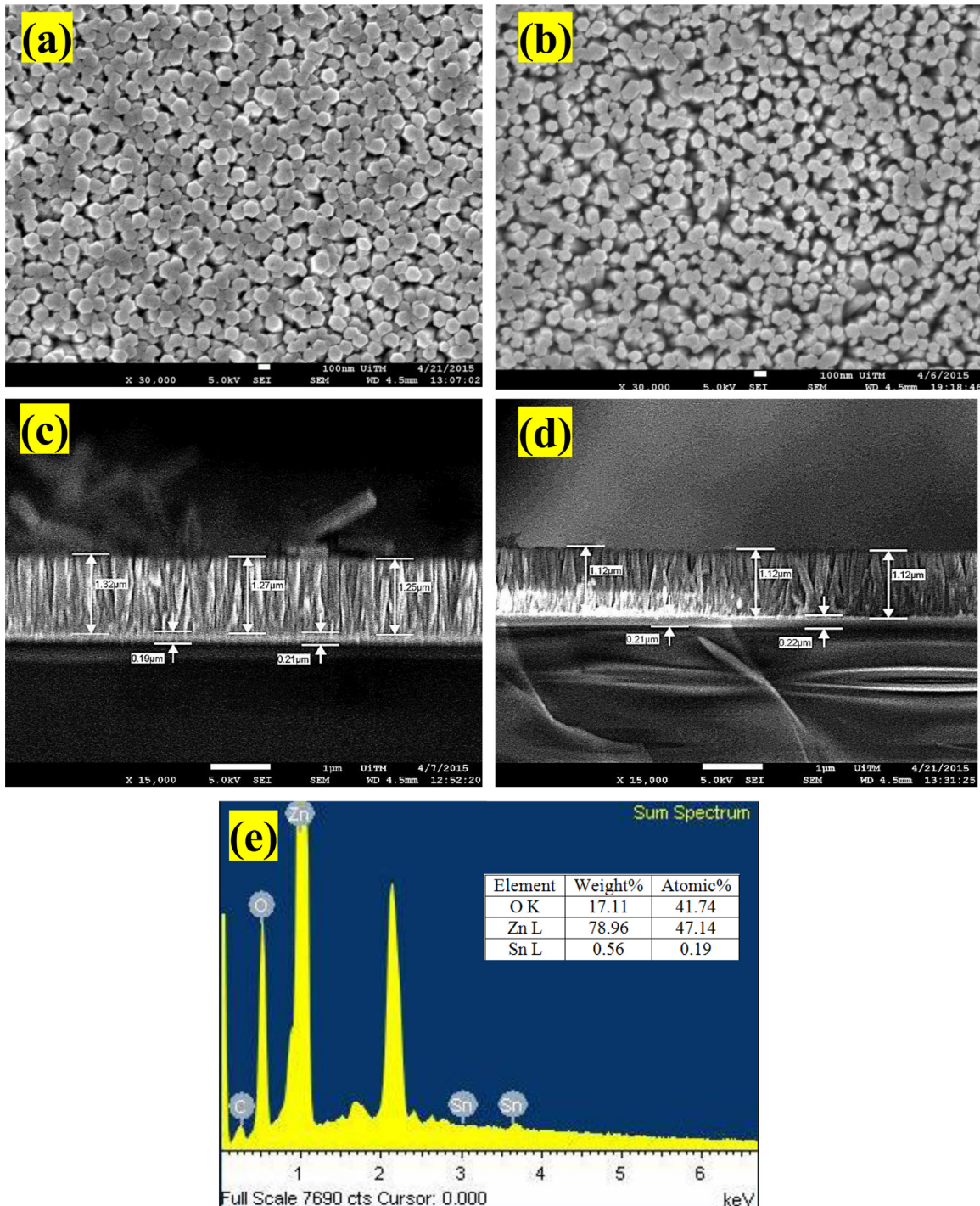


Fig. 3. Surface morphology of (a) undoped ZnO and (b) SZO films prepared through sonicated sol-gel immersion. Cross-sectional images of (c) undoped ZnO and (d) SZO films. (e) EDX spectrum of the SZO film.

undoped ZnO and SZO exhibits hexagonal-shaped structures. The morphology images of the undoped ZnO displayed high uniformity and dense arrays. Similarly, SZO shows uniform and dense arrays, but with a smaller diameter. The surface morphology image of SZO displays the existence of more voids between the nanorods in comparison with undoped ZnO. The diameters of the undoped ZnO and SZO were estimated as 100 and 70 nm on the basis of the FESEM images, respectively. This finding is consistent with the results of the XRD crystallite size depicted in Table 1. Wang et al. demonstrated that the crystallite size of SZO is reduced because the smaller ionic radius of  $\text{Sn}^{4+}$  facilitates the substitution of Zn sites during immersion [46]. The increase in the relative tensile stress from the XRD data of Sn-doped ZnO may induce retraction to the nanorod structure, which tends to produce nanorods with a small diameter.

Fig. 3(c) and (d) shows the cross-sectional images of the undoped ZnO and SZO. The images show that both undoped ZnO and SZO were grown in a vertical alignment with substrates. The average thickness of the nanorod arrays decreases with Sn doping. The average thickness values (nanorods and seed layer) of the undoped ZnO and SZO films were 1.48 and 1.34  $\mu\text{m}$ , respectively. The chemical compositions of SZO were analyzed through EDX, as presented in Fig. 3(e). The EDX spectrum reveals that the film is composed of Zn, O, and Sn. This finding demonstrated that Sn has been successfully doped into the ZnO lattice during growth. The atomic ratio of the Zn:Sn:O was 47.14:0.19:41.74. The existence of a dopant element is consistent with the changes in structural properties, as indicated by the XRD data and FESEM images.

The optical properties of undoped ZnO and SZO films were determined from the transmission and absorption coefficient measurements in the range of 350–800 nm, as shown in Figs. 4 and 5, respectively. Fig. 4 shows the transmittance properties of the undoped ZnO and SZO films. We observed that the transmittance of films slightly decrease with Sn doping. The average transmittances of the undoped ZnO and SZO films in the visible region (400–800 nm) were 63.85% and 61.22%, respectively. Transmission decreased significantly at 380 nm, and this finding corresponds to the band gap energy of ZnO. Fig. 5 shows the absorption coefficient spectra of undoped ZnO and SZO films. The absorption coefficient has been estimated from Lambert's law, as given in the following equation [36]:

$$\alpha = \frac{1}{t} \ln\left(\frac{1}{T}\right) \quad (9)$$

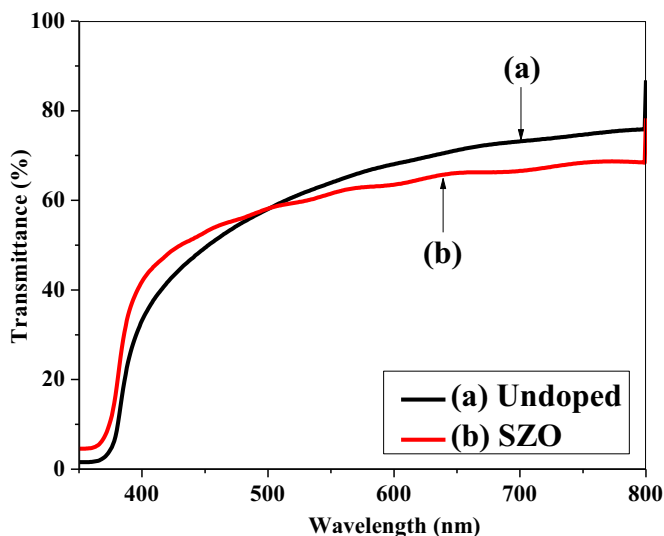


Fig. 4. Transmittance spectra of undoped ZnO and SZO films.

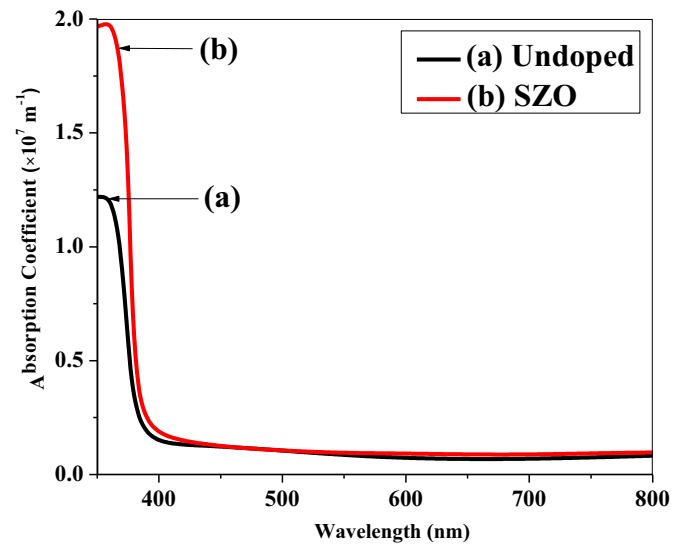


Fig. 5. Plot of absorption coefficient of undoped ZnO and SZO films.

where  $t$  is the thickness of the thin film and  $T$  is the transmittance of the thin film. This figure suggests that both films exhibit high UV absorption properties with sharp absorption edges at wavelengths below 400 nm.

The effect of Sn doping on optical properties can be exposed by the change in optical band gap energy,  $E_g$ .  $E_g$  could be expressed by Tauc's relation as follows [47]:

$$ahv = B(hv - E_g)^{\frac{1}{2}} \quad (10)$$

$$(ahv)^2 = B(hv - E_g) \quad (11)$$

where  $\alpha$  is the absorption coefficient,  $h\nu$  is the photon energy,  $E_g$  is the optical band gap energy, and  $B$  is an energy-independent constant ranging from  $1 \times 10^5$  and  $1 \times 10^6 \text{ cm}^{-1} \text{ eV}^{-1}$ , which is depending on electron–hole mobility [48]. Fig. 6 shows the plot of  $(ahv)^2$  versus the photon energy of the undoped ZnO and SZO.  $E_g$  of the films was obtained from the intercept at the x-axis of the plot. According to Tauc's plot,  $E_g$  of the undoped and SZO films was estimated as 3.20 and 3.22 eV, respectively. We observed that  $E_g$  increases upon Sn doping. The increase in  $E_g$  can be explained by

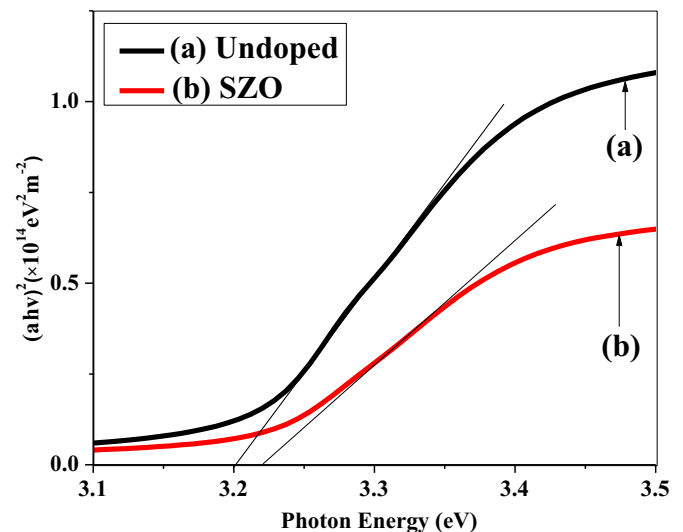


Fig. 6. Estimation of the optical band gap energy,  $E_g$ , undoped ZnO, and SZO films by using Tauc's plot.

Burstein–Moss effect [49]; in this effect,  $E_g$  increases because of band filling that causes Fermi level to move higher than the band edge. In addition,  $E_g$  is dependent on the interatomic spacing of semiconductors, which due to stress alterations in films [36]. R. Ghosh and V. Srikant stated that the increase in  $E_g$  is in phase with the increase in compressive strain/tensile stress along the  $c$ -axis but is inversely related to the increase in tensile strain/compressive stress [50,51]. Normally, the stretched lattice provides a broader  $E_g$  because of the decrease in repulsion between Zn 4s and O 2p bands [50]. This statement supports our XRD results because the compressive strain/tensile stress could be observed in the sample upon Sn doping; as a result,  $E_g$  increased.

The absorption coefficient near the fundamental absorption edge is dependent on the incident photon energy and follows Urbach relation. The occurrence of Urbach relation with band bending is dependent on structural defect [36]. The relation represents Urbach energy,  $E_u$ , where  $E_u$  refers to the width of available localized states in the optical band gap of films.  $E_u$  can be determined according to the following relation [52]:

$$\alpha = \alpha_0 \exp\left(\frac{h\nu}{E_u}\right) \quad (12)$$

where  $\alpha$  is the absorption coefficient,  $\alpha_0$  is the pre-exponential factor,  $h\nu$  is the photon energy, and  $E_u$  is the Urbach energy. Taking the natural logarithm of Eq. (12) yields Eq. (13) below:

$$E_u = \left(\frac{d(\ln \alpha)}{d(h\nu)}\right)^{-1} \quad (13)$$

The Urbach plot of the undoped ZnO and SZO is shown in Fig. 7.  $E_u$  was obtained from the inverse of the slope acquired by fitting the linear division of the respective  $\ln \alpha$  versus  $h\nu$  curves. The estimated  $E_u$  of the undoped ZnO and SZO were 120 and 133 meV, respectively. We observed that  $E_u$  shows an increment as the compressive strain/tensile stress of the crystal structure increases, whereas  $E_g$  changes inversely. The obtained  $E_u$  also supports the increase in dislocation densities and the decreased XRD peak intensities, as discussed previously.

The humidity-sensing response of the undoped ZnO and SZO films, as represented by current ( $I$ ) versus time ( $t$ ) plots, is shown in Fig. 8. Measurement was conducted in a humidity chamber with RH ranging from 40% (initial humidity) to 90% RH and a bias voltage of 5 V at room temperature. RH was changed from 40% to 90%

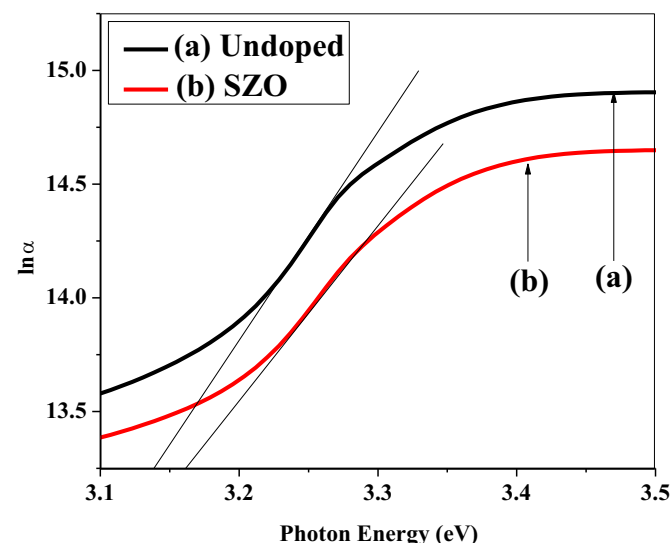
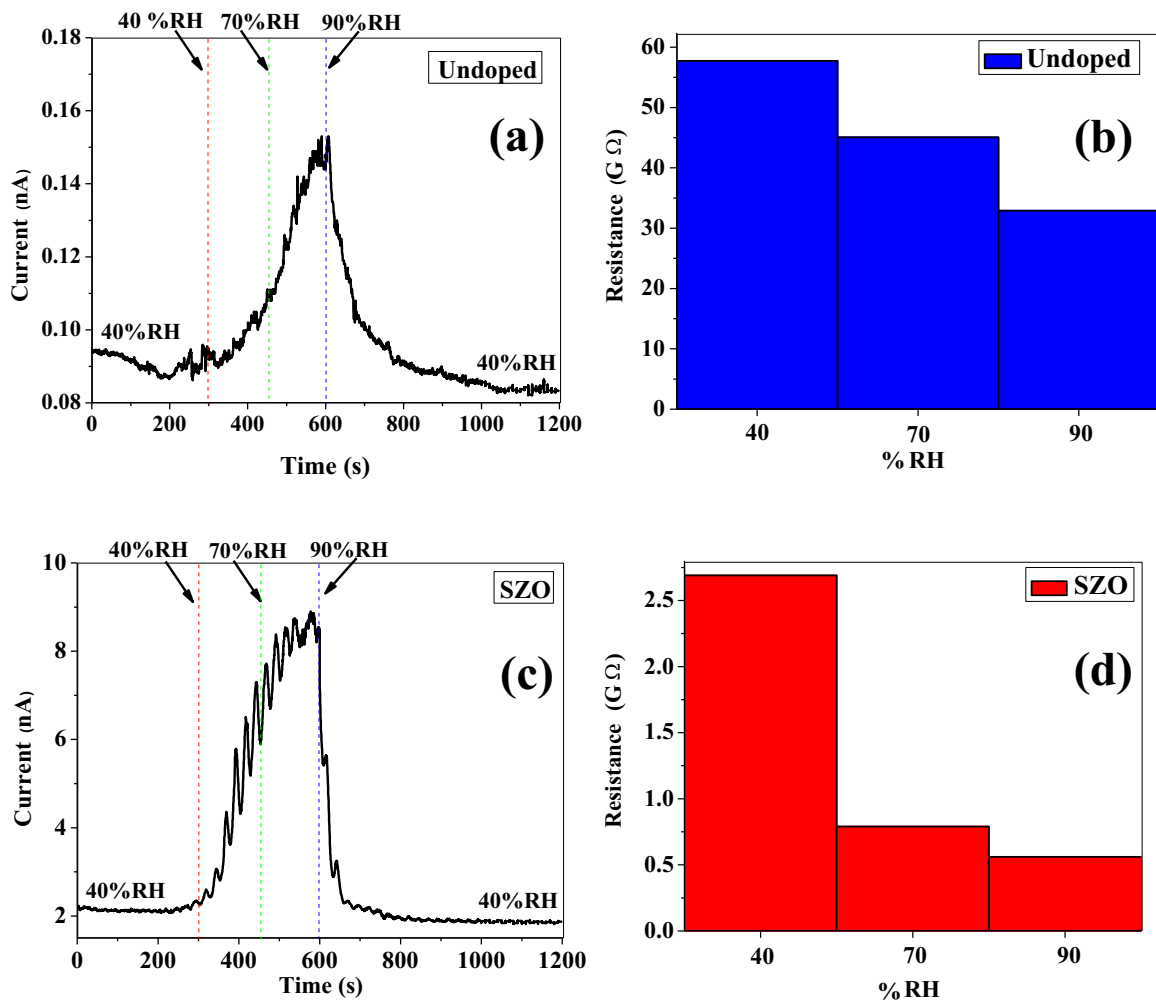


Fig. 7. Plot of  $\ln(\alpha)$  versus photon energy of undoped ZnO and SZO films for Urbach energy estimation.

RH to characterize sensor response toward elevated humidity, and RH was subsequently decreased from 90% to 40% RH for investigating sensor response at decreased humidity. Fig. 8(a) shows the humidity response plot of the undoped ZnO-based humidity sensor at different humidity levels. The figure shows that the undoped ZnO nanorod array-based humidity sensor exhibits poor current signal stability at the low humidity level of 40% RH. At humidity levels ranging from 40% to 70% RH, the current signal gradually increases with a slow response. After a high humidity level of 70% to 90% RH was reached, the sample exhibited high response to humidity and was saturated when humidity reached 90% RH. The current signal gradually decreases when the humidity level was reduced from 90% to 40% RH. The change in resistance value of the undoped ZnO nanorod array-based sensor at elevated humidity levels ranging from 40% to 90% RH are depicted in Fig. 8 (b). The plot was derived by using current signals at elevated humidity levels in Fig. 8(a). These signals are converted into resistance values by using Ohm's law on the basis of a fixed bias voltage of 5 V. The resistance of the undoped ZnO at 40%, 70%, and 90% RH were measured as 57.74, 45.05, and 32.90 G $\Omega$ , respectively. The result suggested that the undoped ZnO nanorod array-based humidity sensor exhibited a slight change in resistance when exposed to different humidity levels from 40% to 70% RH. This pattern is also observed at increased humidity level of 70% to 90% RH.

Fig. 8(c) shows the humidity response plot of the SZO-based humidity sensor at different humidity levels. The result shows that SZO-based humidity sensor exhibits good response in the humidity level ranging from 40% to 70% RH, as shown by a rapid increase in current signal with humidity levels. However, the current signal slightly increased and became saturated when the humidity level increased from 70% to 90% RH. This condition could be due to the generation of ions for ionic and electrolytic conductivities in SZO has become saturated. The surface of SZO may be fully covered through water adsorption; as a result, constant conductivity is obtained at a high humidity level. When humidity level was reduced from 90% to 40% RH, the Sn-doped sample displayed a rapid decrease in current signal compared with that of the undoped ZnO. Fig. 8(d) depicts the resistance plot of the SZO-based humidity sensor at different humidity levels. From the plot, the resistance of SZO at 40%, 70%, and 90% RH were calculated as 2.69, 0.79, and 0.56 G $\Omega$ , respectively. The results clearly show the fast response of the sensor to humidity change from 40% to 70% RH, as shown by the rapid decrease in resistance with humidity levels. However, the resistance slightly changed when humidity level increased from 70% to 90% RH.

From the sensor measurement result in Fig. 8, we can observe that the SZO-based sensor presents a larger current value in comparison with undoped ZnO, as attributed to a larger tensile stress value. By contrast, the undoped ZnO exhibits compressive stress, which contributes to the large resistance of the sample. Shelke et al. reported that compressive stress was observed in the films with higher resistivity [53]. By comparison, tensile stress was detected in lower-resistivity films. In the whole process affected by humidity levels from 40% to 90% RH, the acquired response/recovery times of the undoped ZnO- and SZO-based humidity sensors were 300/350 and 230/30 s, respectively. Response time (adsorption process) and recovery time (desorption process) are obtained by a sensor to achieve or reduce 90% of the total current change. The higher response and recovery times of the undoped ZnO nanorod arrays can be explained by the higher density of nanorods compared with SZO; this finding indicated lower porosities that inhibit water vapor access [31]. Moreover, the small crystallite size and presence of wider pore channels in SZO facilitate a smoother propagation of charge carriers across the surface; as a result, the sensing response/recovery times of the doped arrays were lower than that of the undoped ZnO nanorod arrays. In



**Fig. 8.** Humidity response of (a) undoped ZnO- and (c) SZO-based humidity sensors at humidity level ranging from 40% to 90% RH with 5 V bias. Resistance change in (b) undoped ZnO and (d) SZO samples at different humidity levels (during increased humidity levels).

addition, the surface condition of the undoped ZnO may be less sensitive to humidity than SZO because of the lower electron concentration and lower cationic charge density of  $\text{Zn}^{2+}$  than those of  $\text{Sn}^{4+}$ . The generation of free electrons when doped with Sn and high cationic charge density of  $\text{Sn}^{4+}$ , which is attributed to the smaller ionic radius of  $\text{Sn}^{4+}$  ions in comparison with  $\text{Zn}^{2+}$ , was expected to improve the adsorption/desorption rate of water in SZO. Subsequently, this condition helps to reduce the response and recovery times of the SZO-based sensor.

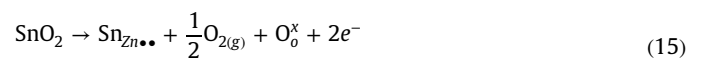
The sensitivity of the undoped ZnO- and SZO-based humidity sensors at two humidity ranges (namely, 40% to 70% RH and 70% to 90% RH) were estimated by using resistance data, as shown in Fig. 8(b) and (d). Sensitivity was quantified by using the following equation [54]:

$$S = \frac{R_a}{R_{rh}} \quad (14)$$

where  $S$  is the sensitivity,  $R_a$  is the resistance of the sensor exposed to the initial humidity level, and  $R_{rh}$  is the resistance of the sensor at the maximum humidity level. These calculations indicated that the undoped ZnO exhibited sensitivities of 1.28 (40% to 70% RH) and 1.40 (70% to 90% RH). SZO yielded sensitivities of 3.41 (40% to 70% RH) and 1.41 (70% to 90% RH). The highest sensitivity produced by SZO at 40% to 70% RH may be attributed to the contribution of SZO to the more porous surface and the smaller crystallite

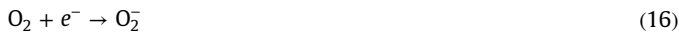
size than those of the undoped ZnO, as estimated on the basis of the FESEM image and XRD data, respectively. This condition enhanced the diffusion of water vapors and increased water adsorption on the nanorod surface. At increased RH level, water adsorbed on the surfaces produce  $\text{H}^+$  ions to the sensing layers. This condition significantly reduced the resistance of the sensor and subsequently increased the sensitivity of the sensor. The resistance of SZO significantly changed because of the more porous surface and the smaller crystallite size of SZO than those of the undoped ZnO; thus, sensitivity was improved. A larger surface area results in a higher content of adsorbed water. As a result, the density of the charge carrier increases, and sensitivity subsequently increased. However, the samples yielded similar sensitivities at humidity levels between 70% and 90% RH possibly because the generation of ions for ionic and electrolytic conductivities in ZnO nanorod arrays has become saturated. The surface of the ZnO nanorod arrays may be fully covered by adsorbed water; as a result, constant conductivity was obtained at a high humidity level.

The results indicated that humidity-sensing performance improved with Sn, particularly at low humidity levels ranging from 40% to 70% RH. Throughout the doping with Sn, more free carriers can be generated, as expressed in the following reaction [55]:



where  $\text{Sn}_{\text{Zn}}^{\bullet\bullet}$  represents two positive charges of Sn ions that

occupy the Zn lattice and act as a donor;  $O_o$  is the oxygen ion in the inherent lattice; and  $x$  represents the neutrality of  $O_o$ . In air with a low humidity level, oxygen molecules are likely adsorbed on the nanorod surface. These oxygen molecules receive free electrons from  $n$ -type ZnO and form negatively charged oxygen species, as shown by following equation [56–58]:



This electron trapping process reduces the carrier concentration in the nanorod arrays and creates the depletion layer on the nanorod surface. The doping with Sn, which generates excessive electrons in the process, increases oxygen adsorption on the nanorod surface. At the beginning, water molecules may replace  $O_2^-$  molecules and release electrons when humidity level was initially increased to 70%, as shown in the following equation:



The released electrons increased the carrier concentration on the nanorod surface, which in turn increased the conductivity of the ZnO nanorod arrays. The conductivity of SZO was increased more rapidly than that of the undoped ZnO nanorod arrays because of the release of more electrons. The depletion layer partially disappeared. In addition, SZO possessed a more porous surface, as observed from the FESEM image in Fig. 3(b), as well as a smaller crystallite and diameter size, as estimated by XRD data and FESEM image, respectively; thus, the surface adsorption of water

molecules is improved [29]. Fig. 9 illustrates the adsorption mechanism of water molecules during initial, intermediate, and final conditions of humidity on the ZnO nanorod array surface. Initially, the adsorbed  $H_2O$  molecules are separated on the ZnO surface. In addition, no hydrogen bonds may be formed among the  $H_2O$  molecules, as can be observed in Fig. 9(a). Therefore, the electrons released through water adsorption mainly contribute to the increase in the conductivity in ZnO nanorod arrays. Thus, the generation of higher carrier concentrations in SZO explained the improvement of humidity sensing than that of the undoped ZnO. As RH further increased up to 70%, the adsorbed water molecules may gradually form a monolayer on the ZnO surface, as shown in Fig. 9 (b). In this stage,  $OH^-$  electrostatically attaches to  $Zn^{2+}$  on the surface and form a chemisorbed layer because of the high electrostatic field produced by  $OH^-$  and  $Zn^{2+}$ . Sn doping improves water adsorption because  $Sn^{4+}$  replaces  $Zn^{2+}$ . This substitution provides more possible reaction sites at the nanorod surface. The surface reaction between the positively charged cationic sides of the metal oxide and water molecules can be expressed as follows [59]:



where  $M^+$  represents positively charged metal ions ( $Zn^{2+}$  and  $Sn^{4+}$ ). Therefore, high charge density regions are created in SZO because of the presence of  $Sn^{4+}$  species, which provide active surface centers for the adsorption of water molecules; as a result,

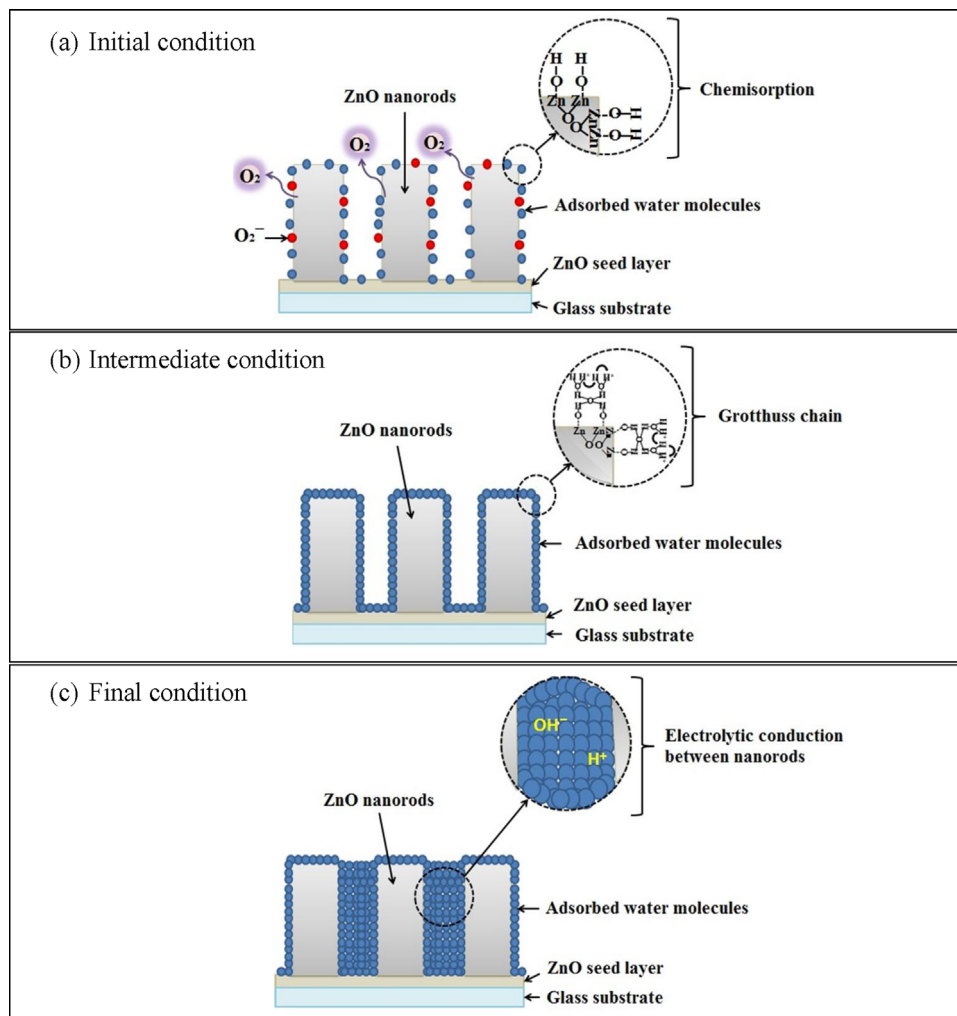


Fig. 9. Water adsorption on the ZnO nanorod array surface at (a) initial (40% RH), (b) intermediate (between 40% to 90% RH), and (c) final (90% RH) humidity levels.

**Table 2**

Response time, recovery time, and sensitivity of undoped ZnO and SZO based humidity sensor.

Sample	Response time (s)	Recovery time (s)	Sensitivity	
			40–70%RH	70–90%RH
Undoped	300	350	1.28	1.40
SZO	230	30	3.41	1.41

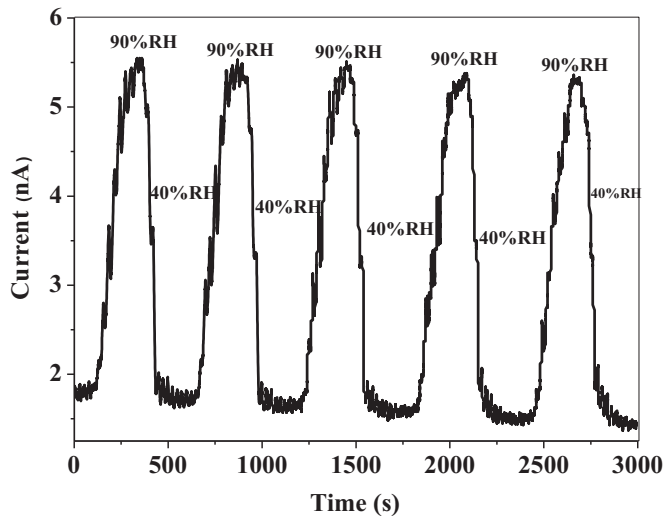
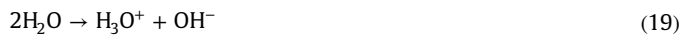


Fig. 10. Repeatability behavior of SZO-based humidity sensor.

highly dense  $H^+$  ions are generated for electrical conduction. This reaction supports the increase in the humidity sensing response of the SZO sample. At a specific RH level, the adsorbed  $H_2O$  molecules can form hydrogen bonds among themselves; thus, water dissociation possibly occurs. This process occurs when the hydroxyl layer forms on top of the chemisorbed layer; thus, another physisorbed layer is formed [60]. Each successive layer of water sticks with the first layer because of hydrogen bonding between the oxygen atom of water molecules and the base hydroxyl layer. The physisorbed water near the chemisorbed water layer can decompose into  $H_3O^+$  and  $OH^-$  ions because of the high electrostatic field in the chemisorbed layer. The protons are generated from the hydration of  $H_3O^+$  to produce  $H^+$  ions at these layers and become the main source of charge carriers across the surface; as a result, surface conductivity significantly changes. This process can be explained by Grotthuss chain, as expressed in the equations below [61]:



Charge conveyance is secured by protonic transfer among hydronium ions ( $H_3O^+$ ). This process is called proton hopping that occurs along a series of hydrogen bonds between hydronium ions and water molecules. These ions provide ionic conductivity, which contributes to the increased conductivity of the ZnO nanorod arrays at high RH. As RH increased to 90% RH, numerous  $H^+$  (or  $H_3O^+$ ) and  $OH^-$  ions are formed, and ionic conductivity may perform a dominant function on nanorod conductivity at high RH, as could be seen in Fig. 9(c). However, at high humidity level, another process involved in the humidity adsorption called capillary condensation is expected to occur [62,63]. At extremely high humidity level, water molecules condense between nanorods. Electrolytic conduction occurs simultaneously with protonic

transport and achieves an equilibrium state because of capillary condensation [64]. This mechanism is supported by the rapid increase in conductivity of the undoped ZnO and SZO samples when RH exceeds 40% RH. Our result revealed that the sensing performance of the SZO sample is more efficient than that of the undoped ZnO possibly because of carrier density and high cationic charge from dopant, pore channels, and small crystallite size. These parameters also provided numerous humidity adsorption sites and promoted easy diffusion. The performance of the undoped ZnO- and SZO-based sensors is summarized in Table 2.

Fig. 10 shows the recycling response of SZO, as measured by repeatedly exposing the film to 40% and 90% RH for five cycles. Nearly identical curves over five cycles were observed in the response plot. This finding indicated that the fabricated humidity sensor was highly stable. The result also demonstrated that the humidity-sensing process with SZO is reversible, with fast response, good repeatability, and stability.

#### 4. Conclusion

SZO was successfully deposited on seed layer-coated glass substrate via sonicated sol-gel immersion method. The XRD pattern revealed that SZO exhibits a wurtzite structure with a preferred (002) plane, which presents a slightly higher intensity than the undoped ZnO. SZO exhibits smaller crystallite size, diameter, and thickness than undoped ZnO does. The SZO film shows compressive strain and tensile stress of  $-0.033\%$  and  $77$  MPa, respectively. The band gap and Urbach energy of SZO were approximately  $3.22$  eV and  $133$  meV, respectively. The sensitivity of the SZO-based sensor was higher than that of the undoped sample. The sensitivities were  $3.41$  and  $1.41$  at  $40\%$  to  $70\%$  RH and  $70\%$  to  $90\%$  RH, respectively. The response and recovery times of the SZO-based humidity sensor also improved to  $230$  and  $30$  s, respectively. This improvement is contributed by high carrier density and cationic charge from Sn dopant, pore channels, and small crystallite size; as a result, humidity adsorption on nanorod arrays is enhanced.

#### Acknowledgments

This work was supported by the Fundamental Research Grant Scheme (FRGS/1/2015/TK04/UITM/02/19 or 600-RMI/FRGS 5/3 (57/2015)) and Long-Term Research Grant Scheme (600-RMI/LRGS 5/3 (3/2013)) from the Ministry of Education Malaysia. The authors also would like to thank the Research Management Institute (RMI) of UiTM and the Ministry of Higher Education of Malaysia for their financial support of this research.

#### References

- [1] M.F. Malek, M.Z. Sahdan, M.H. Mamat, M.Z. Musa, Z. Khusaimi, S.S. Husairi, N.D. Md Sin, M. Rusop, A novel fabrication of MEH-PPV/Al:ZnO nanorod arrays based ordered bulk heterojunction hybrid solar cells, *Appl. Surf. Sci.* 275 (2013) 75–83.
- [2] Y.A. Zhang, Z.H. Chu, X.T. Zhou, T.L. Guo, Efficient field emission characteristics from a planar-gate surface-conduction electron source with ZnO emitters, *J. Alloy. Compd.* 644 (2015) 71–76.
- [3] M.H. Mamat, M.F. Malek, N.N. Hafizah, M.N. Asiah, A.B. Suriani, A. Mohamed, N. Nafarizal, M.K. Ahmad, M. Rusop, Effect of oxygen flow rate on the ultraviolet sensing properties of zinc oxide nanocolumn arrays grown by radio frequency magnetron sputtering, *Ceram. Int.* 42 (2016) 4107–4119.
- [4] M.H. Mamat, M.Z. Sahdan, Z. Khusaimi, A.Z. Ahmed, S. Abdullah, M. Rusop, Influence of doping concentrations on the aluminum doped zinc oxide thin films properties for ultraviolet photoconductive sensor applications, *Opt. Mater.* 32 (2010) 696–699.
- [5] K. Narimani, F.D. Nayeri, M. Kolahdouz, P. Ebrahimi, Fabrication, modeling and simulation of high sensitivity capacitive humidity sensors based on ZnO nanorods, *Sens. Actuators B: Chem.* 224 (2016) 338–343.
- [6] L. Gu, K. Zheng, Y. Zhou, J. Li, X. Mo, G.R. Patzke, G. Chen, Humidity sensors based on ZnO/TiO<sub>2</sub> core/shell nanorod arrays with enhanced sensitivity, *Sens.*

- Actuators B: Chem. 159 (2011) 1–7.
- [7] J. Herrán, I. Fernández, E. Ochoteco, C. Cabañero, H. Grande, The role of water vapour in ZnO nanostructures for humidity sensing at room temperature, *Sens. Actuators B: Chem.* 198 (2014) 239–242.
- [8] C.J. Lin, S.-J. Liao, L.-C. Kao, S.Y.H. Liou, Photoelectrocatalytic activity of a hydrothermally grown branched ZnO nanorod-array electrode for paracetamol degradation, *J. Hazard. Mater.* 291 (2015) 9–17.
- [9] Y. Dou, F. Wu, C. Mao, L. Fang, S. Guo, M. Zhou, Enhanced photovoltaic performance of ZnO nanorod-based dye-sensitized solar cells by using Ga doped ZnO seed layer, *J. Alloy. Compd.* 633 (2015) 408–414.
- [10] J. Lv, P. Yan, M. Zhao, Y. Sun, F. Shang, G. He, M. Zhang, Z. Sun, Effect of ammonia on morphology, wettability and photoresponse of ZnO nanorods grown by hydrothermal method, *J. Alloy. Compd.* 648 (2015) 676–680.
- [11] M.H. Mamat, M.F. Malek, N.N. Hafizah, Z. Khusaimi, M.Z. Musa, M. Rusop, Fabrication of an ultraviolet photoconductive sensor using novel nanostructured, nanohole-enhanced, aligned aluminium-doped zinc oxide nanorod arrays at low immersion times, *Sens. Actuators B: Chem.* 195 (2014) 609–622.
- [12] A. Henni, A. Merrouche, L. Telli, S. Walter, A. Azizi, N. Fenineche, Effect of H<sub>2</sub>O<sub>2</sub> concentration on electrochemical growth and properties of vertically oriented ZnO nanorods electrodeposited from chloride solutions, *Mater. Sci. Semicond. Process.* 40 (2015) 585–590.
- [13] M.H. Mamat, Z. Khusaimi, M.M. Zahidi, A.B. Suriani, Y.M. Siran, S.A.M. Rejab, A. J. Asis, S. Tahiruddin, S. Abdullah, M.R. Mahmood, Controllable growth of vertically aligned aluminum-doped zinc oxide nanorod arrays by sonicated sol-gel immersion method depending on precursor solution volumes, *Jpn. J. Appl. Phys.* 50 (2011) 06GH04.
- [14] A. Sáenz-Trevizo, P. Amézaga-Madrid, P. Pizá-Ruiz, W. Antúnez-Flores, C. Ornelas-Gutiérrez, M. Miki-Yoshida, Single and multi-layered core-shell structures based on ZnO nanorods obtained by aerosol assisted chemical vapor deposition, *Mater. Charact.* 105 (2015) 64–70.
- [15] M.H. Mamat, N.N. Hafizah, M. Rusop, Fabrication of thin, dense and small-diameter zinc oxide nanorod array-based ultraviolet photoconductive sensors with high sensitivity by catalyst-free radio frequency magnetron sputtering, *Mater. Lett.* 93 (2013) 215–218.
- [16] B. Wu, Y. Zhang, Z. Shi, X. Li, X. Cui, S. Zhuang, B. Zhang, G. Du, Different defect levels configurations between double layers of nanorods and film in ZnO grown on c-Al<sub>2</sub>O<sub>3</sub> by MOCVD, *J. Lumin.* 154 (2014) 587–592.
- [17] V. Ruiz, I. Fernández, P. Carrasco, G. Cabañero, H.J. Grande, J. Herrán, Graphene quantum dots as a novel sensing material for low-cost resistive and fast-response humidity sensors, *Sens. Actuators B: Chem.* 218 (2015) 73–77.
- [18] R. Gao, D.-f Lu, J. Cheng, Y. Jiang, L. Jiang, Z.-m Qi, Humidity sensor based on power leakage at resonance wavelengths of a hollow core fiber coated with reduced graphene oxide, *Sens. Actuators B: Chem.* 222 (2016) 618–624.
- [19] X.-d Lan, S.-y Zhang, Y. Wang, L. Fan, X.-j Shui, Humidity responses of Love wave sensors based on ZnO/R-sapphire bilayer structures, *Sens. Actuators A: Phys.* 230 (2015) 136–141.
- [20] N. Sakly, A. Haj Said, H. Ben Ouada, Humidity-sensing properties of ZnO QDs coated QCM: Optimization, modeling and kinetic investigations, *Mater. Sci. Semicond. Process.* 27 (2014) 130–139.
- [21] K. Jiang, T. Fei, F. Jiang, G. Wang, T. Zhang, A dew sensor based on modified carbon black and polyvinyl alcohol composites, *Sens. Actuators B: Chem.* 192 (2014) 658–663.
- [22] L. Xu, G. Zheng, L. Zhao, S. Pei, Two different mechanisms on UV emission enhancement in Ag-doped ZnO thin films, *J. Lumin.* 158 (2015) 396–400.
- [23] L. Zamora, J.C. Paz, J.F. Piamba, J.A. Tabares, G.A.P. Alcázar, A Mössbauer and magnetic study of ball milled Fe-doped ZnO Powders, *Hyperfine Interact.* 232 (2015) 111–118.
- [24] D. Miao, H. Hu, L. Gan, Fabrication of high infrared reflective Al-doped ZnO thin films through electropulsing treatment for solar control, *J. Alloy. Compd.* 639 (2015) 400–405.
- [25] C. Manoharan, G. Pavithra, S. Dhanapandian, P. Dhamodaran, B. Shanthi, Properties of spray pyrolysed ZnO:Sn thin films and their antibacterial activity, *Spectrochim. Acta A: Mol. Biomol. Spectrosc.* 141 (2015) 292–299.
- [26] K. Soonjae, N. Sekwon, J. Haseok, K. Sunho, L. Byunghoon, Y. Jaehyun, K. Hyoungsub, L. Hoo-Jeong, Effects of Sn doping on the growth morphology and electrical properties of ZnO nanowires, *Nanotechnology* 24 (2013) 065703.
- [27] X. Zhou, T. Lin, Y. Liu, C. Wu, X. Zeng, D. Jiang, Y.-a Zhang, T. Guo, Structural, optical, and improved field-emission properties of tetrapod-shaped Sn-doped ZnO nanostructures synthesized via thermal evaporation, *ACS Appl. Mater. Interfaces* 5 (2013) 10067–10073.
- [28] A.A. Hendi, R.H. Alorainy, F. Yakuphanoglu, Humidity sensing characteristics of Sn doped Zinc oxide based quartz crystal microbalance sensors, *J. Sol.-Gel Sci. Technol.* 72 (2014) 559–564.
- [29] T. Ates, C. Tatar, F. Yakuphanoglu, Preparation of semiconductor ZnO powders by sol-gel method: Humidity sensors, *Sens. Actuators A: Phys.* 190 (2013) 153–160.
- [30] M.F. Malek, M.H. Mamat, M.Z. Musa, Z. Khusaimi, M.Z. Sahdan, A.B. Suriani, A. Ishak, I. Saurdi, S.A. Rahman, M. Rusop, Thermal annealing-induced formation of ZnO nanoparticles: Minimum strain and stress ameliorate preferred c-axis orientation and crystal-growth properties, *J. Alloy. Compd.* 610 (2014) 575–588.
- [31] P. Pascariu, A. Airinei, N. Oлару, I. Petrila, V. Nica, L. Sacarescu, F. Tudorache, Microstructure, electrical and humidity sensor properties of electrospun NiO-SnO<sub>2</sub> nanofibers, *Sensors Actuators B: Chem.* 222 (2016) 1024–1031.
- [32] S.K. Mishra, S. Bayan, R. Shankar, P. Chakraborty, R.K. Srivastava, Efficient UV photosensitive and photoluminescence properties of sol-gel derived Sn doped ZnO nanostructures, *Sens. Actuators A: Phys.* 211 (2014) 8–14.
- [33] F. Gao, X.Y. Liu, L.Y. Zheng, M.X. Li, Y.M. Bai, J. Xie, Microstructure and optical properties of Fe-doped ZnO thin films prepared by DC magnetron sputtering, *J. Cryst. Growth* 371 (2013) 126–129.
- [34] A.A. Al-Ghamdi, O.A. Al-Hartomy, M. El Okr, A.M. Nawar, S. El-Gazzar, F. El-Tantawy, F. Yakuphanoglu, Semiconducting properties of Al doped ZnO thin films, *Spectrochim. Acta A: Mol. Biomol. Spectrosc.* 131 (2014) 512–517.
- [35] T. Jan, J. Iqbal, M. Ismail, Q. Mansoor, A. Mahmood, A. Ahmad, Eradication of multi-drug resistant bacteria by Ni doped ZnO nanorods: structural, Raman and optical characteristics, *Appl. Surf. Sci.* 308 (2014) 75–81.
- [36] M.F. Malek, M.H. Mamat, M.Z. Musa, T. Soga, S.A. Rahman, S.A.H. Alrokayan, H. A. Khan, M. Rusop, Metamorphosis of strain/stress on optical band gap energy of ZAO thin films via manipulation of thermal annealing process, *J. Lumin.* 160 (2015) 165–175.
- [37] C. Wang, S. Ma, A. Sun, R. Qin, F. Yang, X. Li, F. Li, X. Yang, Characterization of electrospun Pr-doped ZnO nanostructure for acetic acid sensor, *Sens. Actuators B: Chem.* 193 (2014) 326–333.
- [38] M. Yao, F. Ding, Y. Cao, P. Hu, J. Fan, C. Lu, F. Yuan, C. Shi, Y. Chen, Sn doped ZnO layered porous nanocrystals with hierarchical structures and modified surfaces for gas sensors, *Sens. Actuators B: Chem.* 201 (2014) 255–265.
- [39] P.S. Shewale, Y.S. Yu, J.H. Kim, C.R. Bobade, M.D. Uplane, H<sub>2</sub>S gas sensitive Sn-doped ZnO thin films: synthesis and characterization, *J. Anal. Appl. Pyrolysis* 112 (2015) 348–356.
- [40] M. Gao, X. Wu, J. Liu, W. Liu, The effect of heating rate on the structural and electrical properties of sol-gel derived Al-doped ZnO films, *Appl. Surf. Sci.* 257 (2011) 6919–6922.
- [41] M.F. Malek, M.H. Mamat, Z. Khusaimi, M.Z. Sahdan, M.Z. Musa, A.R. Zainun, A. B. Suriani, N.D. Md Sin, S.B. Abd Hamid, M. Rusop, Sonicated sol-gel preparation of nanoparticulate ZnO thin films with various deposition speeds: the highly preferred c-axis (0 0 2) orientation enhances the final properties, *J. Alloy. Compd.* 582 (2014) 12–21.
- [42] D. Fang, K. Lin, T. Xue, C. Cui, X. Chen, P. Yao, H. Li, Influence of Al doping on structural and optical properties of Mg-Al co-doped ZnO thin films prepared by sol-gel method, *J. Alloy. Compd.* 589 (2014) 346–352.
- [43] N. Chahmat, T. Souier, A. Mokri, M. Bououina, M.S. Aida, M. Ghers, Structure, microstructure and optical properties of Sn-doped ZnO thin films, *J. Alloy. Compd.* 593 (2014) 148–153.
- [44] G. Turgut, E. Sönmez, A study of Pb-doping effect on structural, optical, and morphological properties of ZnO thin films deposited by sol-gel spin coating, *Metall. Mater. Trans. A* 45 (2014) 3675–3685.
- [45] K. Raja, P.S. Ramesh, D. Geetha, Structural, FTIR and photoluminescence studies of Fe doped ZnO nanopowder by co-precipitation method, *Spectrochim. Acta A: Mol. Biomol. Spectrosc.* 131 (2014) 183–188.
- [46] H. Wang, R. Bhattacharjee, I.M. Hung, L. Li, R. Zeng, Material characteristics and electrochemical performance of Sn-doped ZnO spherical-particle photoanode for dye-sensitized solar cells, *Electrochim. Acta* 111 (2013) 797–801.
- [47] M. Ilassi, I. Sta, M. Hajji, H. Ezzaouia, Effect of nickel doping on physical properties of zinc oxide thin films prepared by the spray pyrolysis method, *Appl. Surf. Sci.* 301 (2014) 216–224.
- [48] E.A. Davis, N.F. Mott, Electrical and transparent properties of amorphous semiconductor, *Philos. Mag.* 22 (1970) 903–920.
- [49] S.D. Senol, O. Ozturk, C. Terzioğlu, Effect of boron doping on the structural, optical and electrical properties of ZnO nanoparticles produced by the hydrothermal method, *Ceram. Int.* 41 (2015) 11194–11201.
- [50] R. Ghosh, D. Basak, S. Fujihara, Effect of substrate-induced strain on the structural, electrical, and optical properties of polycrystalline ZnO thin films, *J. Appl. Phys.* 96 (2004) 2689–2692.
- [51] V. Srikanth, D.R. Clarke, Optical absorption edge of ZnO thin films: The effect of substrate, *J. Appl. Phys.* 81 (1997) 6357–6364.
- [52] C. Shin, S.M. Iftiqar, J. Park, Y. Kim, S. Baek, J. Jang, M. Kim, J. Jung, Y. Lee, S. Kim, J. Yi, Optimization of intrinsic hydrogenated amorphous silicon deposited by very high-frequency plasma-enhanced chemical vapor deposition using the relationship between Urbach energy and silane depletion fraction for solar cell application, *Thin Solid Films* 547 (2013) 256–262.
- [53] V. Shelke, B.K. Sonawane, M.P. Bhole, D.S. Patil, Electrical and optical properties of transparent conducting tin doped ZnO thin films, *J. Mater. Sci.: Mater. Electron* 23 (2012) 451–456.
- [54] N.D. Md Sin, M.H. Mamat, M.F. Malek, M. Rusop, Fabrication of nanocubic ZnO/SnO<sub>2</sub> film-based humidity sensor with high sensitivity by ultrasonic-assisted solution growth method at different Zn:Sn precursor ratios, *Appl. Nanosci.* 4 (2014) 829–838.
- [55] F.J. Sheini, D.S. Joag, M.A. More, Electrochemical synthesis of Sn doped ZnO nanowires on zinc foil and their field emission studies, *Thin Solid Films* 519 (2010) 184–189.
- [56] C. Lai, X. Wang, Y. Zhao, H. Fong, Z. Zhu, Effects of humidity on the ultraviolet nanosensors of aligned electrospun ZnO nanofibers, *RSC Adv.* 3 (2013) 6640–6645.
- [57] C.-L. Hsu, K.-C. Chen, T.-Y. Tsai, T.-J. Hsueh, Fabrication of gas sensor based on p-type ZnO nanoparticles and n-type ZnO nanowires, *Sens. Actuators B: Chem.* 182 (2013) 190–196.
- [58] C.-L. Hsu, H.-H. Li, T.-J. Hsueh, Water- and humidity-enhanced UV detector by using p-type La-doped ZnO nanowires on flexible polyimide substrate, *ACS Appl. Mater. Interfaces* 5 (2013) 11142–11151.
- [59] S. Sikarwar, B.C. Yadav, Opto-electronic humidity sensor: a review, *Sens. Actuators A: Phys.* 233 (2015) 54–70.
- [60] M. Balde, A. Vena, B. Sorli, Fabrication of porous anodic aluminum oxide layers

- on paper for humidity sensors, *Sens. Actuators B: Chem.* 220 (2015) 829–839.
- [61] J.-L. Hou, C.-H. Wu, T.-J. Hsueh, Self-biased ZnO nanowire humidity sensor vertically integrated on triple junction solar cell, *Sens. Actuators B: Chem.* 197 (2014) 137–141.
- [62] S. Jagtap, K.R. Priolkar, Evaluation of ZnO nanoparticles and study of ZnO–TiO<sub>2</sub> composites for lead free humidity sensors, *Sens. Actuators B: Chem.* 183 (2013) 411–418.
- [63] P.M. Faia, J. Libardi, C.S. Louro, Effect of V<sub>2</sub>O<sub>5</sub> doping on p-to n-conduction type transition of TiO<sub>2</sub>:WO<sub>3</sub> composite humidity sensors, *Sens. Actuators B: Chem.* 222 (2016) 952–964.
- [64] P.M. Faia, C.S. Furtado, A.J. Ferreira, AC impedance spectroscopy: a new equivalent circuit for titania thick film humidity sensors, *Sens. Actuators B: Chem.* 107 (2005) 353–359.